

Coexisting Non-Trivial Van der Waals Magnetic Orders Enable Field-Free Spin-Orbit Torque Magnetization Dynamics

Bing Zhao,* Lakhan Bainsla, Soheil Ershadrad, Lunjie Zeng, Roselle Ngalyo, Peter Svedlindh, Eva Olsson, Biplob Sanyal,* and Saroj P. Dash*

The discovery of van der Waals (vdW) magnetic materials exhibiting non-trivial and tunable magnetic interactions can lead to exotic magnetic states that are not readily attainable with conventional materials. Such vdW magnets can provide a unique platform for studying new magnetic phenomena and realizing magnetization dynamics for energy-efficient and non-volatile spintronic memory and computing technologies. Here, the coexistence of ferromagnetic and antiferromagnetic orders in vdW magnet ($\text{Co}_{0.5}\text{Fe}_{0.5}$)_{5-x}GeTe₂ (CFGF) above room temperature, inducing an intrinsic exchange bias and canted perpendicular magnetism is discovered. Such non-trivial intrinsic magnetic order enables to realize energy-efficient, magnetic field-free, and deterministic spin-orbit torque (SOT) switching of CFGF in heterostructure with Pt. These experiments, in conjunction with density functional theory and Monte Carlo simulations, demonstrate the coexistence of non-trivial magnetic orders in CFGF, which enables field-free SOT magnetization dynamics in spintronic devices.

also for the next generation of memory, logic, communication, and beyond von Neumann computing technologies.^[1,2] Such non-trivial magnetic states are required for efficient control of spin-orbit torque (SOT) magnetization dynamics phenomena in spintronic devices for non-volatile information and communication technologies.^[3–5] However, for energy-efficient and field-free SOT magnetization switching, the discovery of new materials and methods is needed for enhanced control over the device parameters.^[2,6–17] One of the strategies is to utilize heterostructures of ferromagnetic (FM) and antiferromagnetic (AFM) materials with exchange bias to realize field-free SOT magnetization switching.^[7,8,18,19] However, there are challenges in fabricating high-quality FM/AFM interfaces with traditional multilayers, and the discovery of a single material with coexisting

magnetic orders is necessary. In addition to conventional thin films, recently vdW FM/AFM heterostructures have been used to show field-free SOT switching.^[19] However, achieving such

1. Introduction

Exploring new strategies to realize new non-trivial magnetic orders is of great importance for fundamental magnetism, and

B. Zhao, L. Bainsla, R. Ngalyo, S. P. Dash
 Department of Microtechnology and Nanoscience
 Chalmers University of Technology
 Göteborg SE-41296, Sweden
 E-mail: zbing@chalmers.se; saroj.dash@chalmers.se

L. Bainsla
 Department of Physics
 Indian Institute of Technology Ropar
 Roopnagar 140001, India
 S. Ershadrad, B. Sanyal
 Department of Physics and Astronomy
 Uppsala University
 Box 516, Uppsala 75120, Sweden
 E-mail: biplab.sanyal@physics.uu.se

L. Zeng, E. Olsson
 Department of Physics
 Chalmers University of Technology
 Göteborg 41296, Sweden

P. Svedlindh
 Department of Materials Science and Engineering
 Uppsala University
 Uppsala SE-751 03, Sweden

S. P. Dash
 Wallenberg Initiative Materials Science for Sustainability
 Department of Microtechnology and Nanoscience
 Chalmers University of Technology
 Göteborg SE-41296, Sweden

S. P. Dash
 Graphene Center
 Chalmers University of Technology
 Göteborg SE-41296, Sweden

 The ORCID identification number(s) for the author(s) of this article can be found under <https://doi.org/10.1002/adma.202502822>

© 2025 The Author(s). Advanced Materials published by Wiley-VCH GmbH. This is an open access article under the terms of the [Creative Commons Attribution](https://creativecommons.org/licenses/by/4.0/) License, which permits use, distribution and reproduction in any medium, provided the original work is properly cited.

DOI: 10.1002/adma.202502822

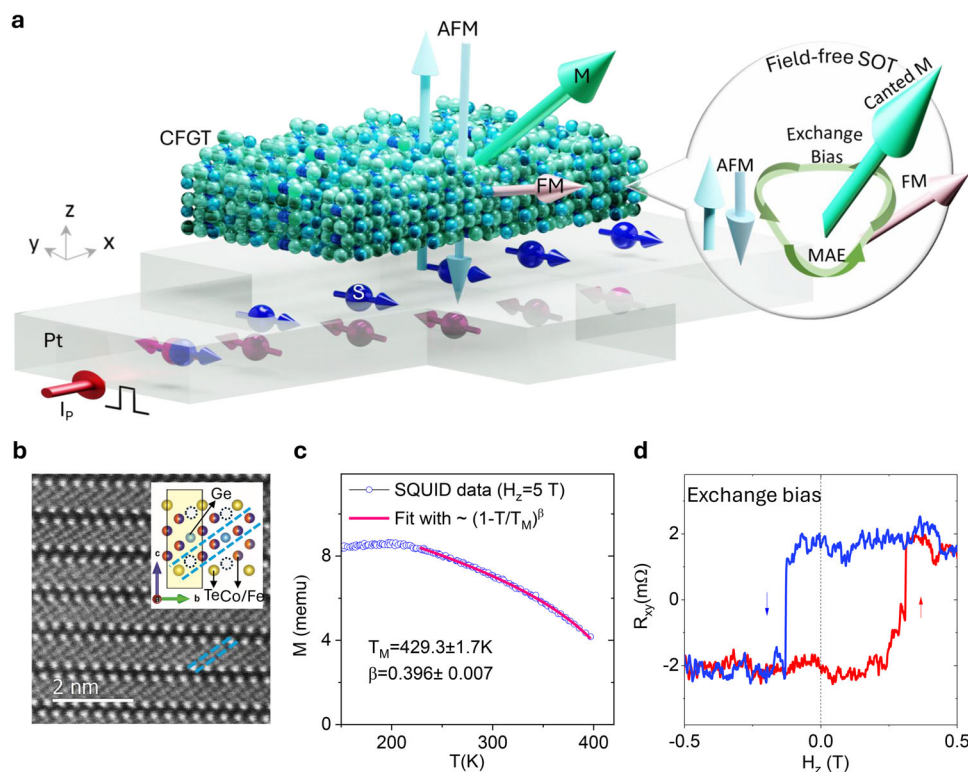


Figure 1. Coexistence of ferro- and antiferro-magnetic orders in a single atomic stacking nanolayers of $(\text{Co}_{0.5}\text{Fe}_{0.5})_{5-x}\text{GeTe}_2$. a) Schematics of CFGT/Pt van der Waals heterostructure used for spin-orbit torque (SOT) experiments. The ferro- (FM) and antiferro-magnetic (AFM) orders in a single atomic stacking nanolayers, creating a net canted magnetization M with exchange bias interaction and magnetocrystalline anisotropy energy (MAE) (in the inset), which is useful for field-free SOT switching. The charge current I_p applied to Pt generates a spin current J_s with spin polarizations S_y due to the spin Hall effect. b) Atomic resolution high angle annular dark field (HAADF) scanning transmission electron microscopy (STEM) images of CFGT. The inset is the atomic model projection along the bc -plane. The dashed cycle represents Fe_1 site vacancies. c) Temperature dependence of the magnetization M of bulk CFGT measured with a fixed out-of-plane magnetic field of 5T. The magnetic order temperature T_M is extracted with $\sim (1-T/T_{C(N)})^\beta$ with critical factor β .^[28,29] d) A representative AHE signal at 300 K with clear exchange bias effect ($H_{\text{EB}} = +75$ mT) after subtraction of a linear background at a ± 0.6 T field range.

phenomena in a single material will be a breakthrough for SOT memory technology.

Recently discovered two-dimensional van der Waals (vdW) magnetic materials have significant potential for such unique non-trivial magnetic states in a single material because of their low dimensionality, tunable magnetic anisotropy (MA), proximity-induced interactions, and potential for voltage-controlled magnetism and multi-functionalities of SOT devices.^[2,20–27] Furthermore, it is possible to create unique, non-trivial spin ordering by controlling the intra- and interlayer magnetic exchange coupling inherent to vdW materials, as well as the MA that depends on atomic position and stacking; however, this has not been explored.

Here, we discover non-trivial spin ordering with the coexistence of FM and AFM magnetic ordering in single vdW magnet $(\text{Co}_{0.5}\text{Fe}_{0.5})_{5-x}\text{GeTe}_2$ (CFGT), accompanied by a pronounced exchange bias effect and canted magnetization that persists above room temperature (see Figure 1a), which is not readily attainable with conventional materials. By tuning the symmetry of the Fe_1 -site vacancies, we successfully introduced a FM order in an AFM system. To understand the correlation between structural properties and the coexistence of FM and AFM orderings, we performed high-throughput density functional theory (DFT) calculations

and Monte Carlo simulations. This unique intrinsic canted magnetism of vdW magnet CFGT enables an energy-efficient and deterministic field-free spin-orbit torque (SOT)-induced magnetization switching when integrated with Pt in a heterostructure, owing to its high charge-spin conversion efficiency, superior electrical conductance, and excellent spin transparency at the interface (see Figure 1a, inset).

2. Results and Discussion

2.1. Coexistence of Ferromagnetic and Antiferromagnetic Orders in CFGT at Room Temperature: Exchange Bias and Canted Magnetism

The motivation behind using the vdW magnet CFGT is its beyond room-temperature magnetic orders and tunable magnetic properties depending on atomic positions, stacking, and intra- and interlayer magnetic interactions.^[26,27,30] Fe_5GeTe_2 exhibits an ABC stacking arrangement, characterized by a rhombohedral unit cell and belonging to the $R\bar{3}m$ space group.^[26,27] By substituting around 50% of the Fe atoms with Co, crystals of CFGT alloy were synthesized.^[26,27,30] To characterize the atomic structure of CFGT, we performed high-resolution scanning

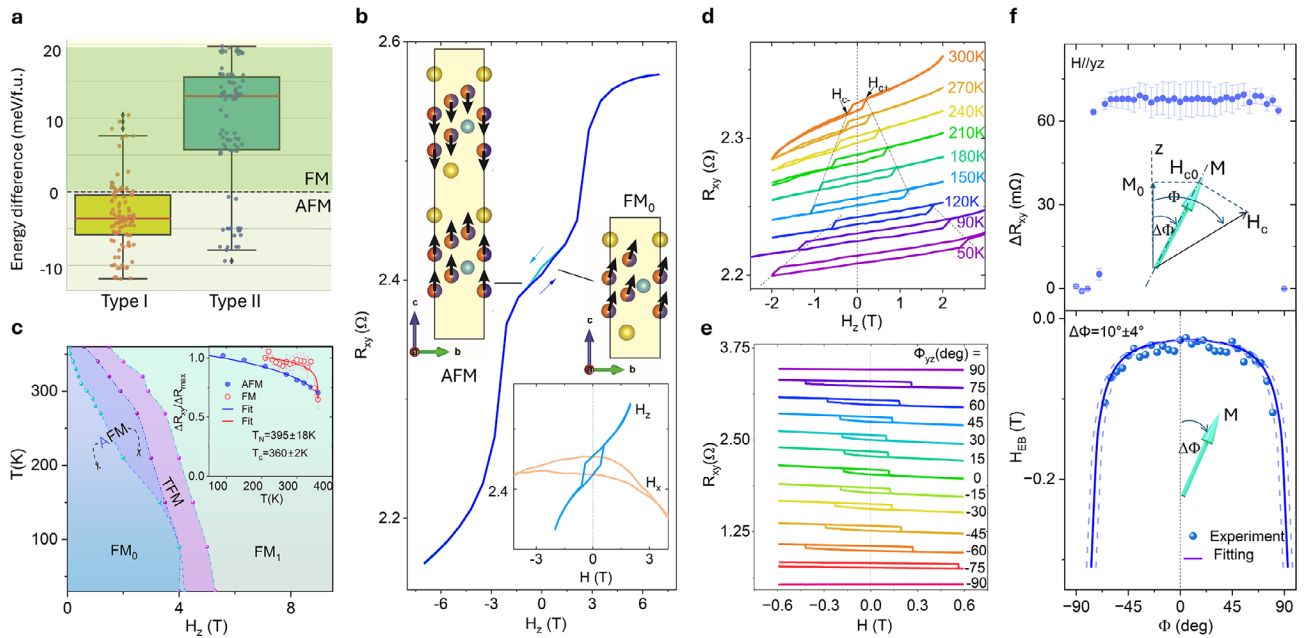


Figure 2. Origin of the (A) FM magnetic orders and the canted magnetization M in $(\text{Co}_{0.5}\text{Fe}_{0.5})_{1-x}\text{GeTe}_2$ nanolayers. a) Boxplots of the magnetic ground state distribution of AFM (FM) orders in CFGT, where each dot represents a distinct Co distribution. The orange lines are the statistically averaged results. b) Transversal Hall resistance (AHE) $R_{xy} = V_{xy}/I$ of a CFGT nanolayers as a function of the out-of-plane field (H_z) at 300 K in the field range of ± 8 Tesla. The blue/green arrows show the AFM and FM magnetic spin configurations. The schematics show the magnetic states near 0 T. Inset: AHE signals at 300 K in a smaller field range with $H_z(x)$. c) Phase diagram of the CFGT nanolayers as a function of H_z and T . Inset shows the temperature evolution of the normalized AFM and FM components. The Curie (Néel) temperature $T_{C(N)}$ is extracted by fitting with $\approx (1-T/T_{C(N)})^\beta$. d) AHE signals R_{xy} with out-of-plane field H_z at different temperatures in the low field range. $H_{c\pm}$ are the coercive fields in positive/negative directions. The dashed lines are guide to the eye. e) AHE signals R_{xy} with magnetic field sweep at different yz -plane angles Φ measured at 300 K. f) The magnitude of the AHE signal ΔR_{xy} and exchange bias field $H_{EB} = (H_{c+} + H_{c-})/2$ as a function of the yz -plane angle Φ . The purple curve in the bottom panel is a fit with uncertainty represented by dashed curves. The insets show the schematics of the magnetization M at a canting angle $\Delta\Phi$ and its relationship with the external field H_c .

transmission electron microscopy (STEM) measurements as shown in Figure 1b (see details in Experimental and Note S1 and Figure S1, Supporting Information). We observe a uniform and homogeneous unique AA atomic crystal structure,^[30] with two different types of Fe_1 -site atomic vacancy positions – an antisymmetric (type I) and a symmetric (type II) crystal structure with Fe_1 deficiency sites (see more detailed analysis in Note S2, Figure S2, and Table S1, Supporting Information). Figure 1c shows the temperature-dependent SQUID measurements as a function of a fixed out-of-plane field, confirming the magnetic behavior of CFGT with a magnetic order temperature $T_M = 429.3 \pm 1.7$ K.

To investigate the magnetic properties of thin CFGT nanolayers, magnetotransport measurements using the anomalous Hall effect (AHE) were conducted on nanofabricated Hall-bar devices (see Experimental section). Figure 1d shows AHE data (Hall resistance R_{xy} as a function of the out-of-plane magnetic field H_z) at 300 K, revealing a clear hysteresis loop that confirms the presence of out-of-plane ferromagnetism in CFGT with finite remanence and coercivity at room temperature. More interestingly, a strong exchange bias effect is observed, which is manifested as a horizontal shift in the magnetic hysteresis loop due to the coexistence of intrinsic FM and AFM ordering in CFGT. Our density functional theory (DFT) calculations also show the coexistence of FM and AFM magnetic states. The boxplots in Figure 2a illustrate these structural dependencies of calculated magnetic ground states, where each dot represents a distinct Co distribu-

tion. The y-axis shows the energy difference between FM and AFM ordering for each configuration. Negative values indicate a preference for AFM order, while positive values correspond to FM order in the unit cell. We have calculated hundreds of different possible Co-doping cases for Type I (II) structures. The statistically averaged results suggest that the Type I (II) structures with all possible Co doping show the AFM (FM) ground magnetic state, respectively (see details in Note S3 and Table S2, Supporting Information). The detailed AHE measurements of CFGT nanolayers in both low and high field ranges confirmed the coexistence of FM and AFM states at room temperature below the spin-flip transition, as shown in Figure 2b. From both experiments and theoretical analysis, we observe that our CFGT sample is primarily in the AFM state, and we introduced a coexisting FM state due to the presence of symmetric Fe_1 vacancy sites. We further evaluated the temperature evolution of the FM (AFM) magnetic orders (Figure S3, Supporting Information). The extracted magnetic phase diagram for the CFGT nanolayers as a function of H_z and temperature T is shown in Figure 2c. In a small field range, the FM_0 and AFM orders coexist. A transitional magnetic order (TFM) appears when the field is large enough to re-align the AFM components. Finally, both AFM and FM_0 magnetic orders are aligned with the external field direction to form the ferromagnetic FM_1 order. Based on the evolution of magnitude of AFM(FM) components in the AHE signals (Figure 2c, inset), we extract the Curie (Néel) temperature $T_C = 360 \pm 2$ K ($T_N = 395$

± 15 K) of CFGT nanolayers. Furthermore, Figure 2d illustrate a more detailed temperature evolution of the AHE signal, where apparent hysteresis is observed in a smaller magnetic field sweep, i.e., with the ferromagnetic FM_0 order. At lower temperatures, the coercivity $H_{c\pm}$ increases, and the exchange bias effect becomes more prominent below 150 K. To be noted, the Curie temperature (T_c) for the ferromagnetic orders in CFGT is around 429 K for bulk samples and 360 K for nanolayers, among the highest T_c among all the known 2D vdW magnets (like Fe_3GaTe_2 ,^[31] Fe_3GeTe_2 ,^[32] Fe_3GeTe_2 ,^[33] $CrTe_2$,^[34] CrI_3 ,^[35] etc. see Figure S12b, Supporting Information).

Due to the coexistence of both FM and AFM properties in CFGT nanolayers, there is a possibility that its MA may be significantly impacted. To examine this, we conducted an angle-dependence study of the AHE on the CFGT Hall-bar device at room temperature (Figure 2e). The AHE signal with exchange bias effect can be observed at all angles, except for the almost in-plane case $\Phi \approx \pm 90$ deg where the signal vanishes due to no effective field to switch the M . As shown in Figure 2e, the magnitude of the AHE signal remains almost constant at all field sweep angles Φ , indicating a strong MA and minimal rotation of the magnetization towards the field direction in the range of ± 600 mT. The extracted exchange bias field H_{EB} at different angles is presented in Figure 2f (bottom panel). We consider H_{c0} to be the intrinsic coercive field required to switch M with a magnetic field aligned with the easy axis of the magnetization. The projection of the nominal coercive field $H_c(\Phi)$ at field sweep angle Φ on the easy axis must be equal to H_{c0} , that is, $H_{c0} = H_c \cos(\Phi - \Delta\Phi)$, where $\Delta\Phi$ defines the canted angle of the magnetization easy axis (Figure 2e, insets schematics). Then the relation $H_{EB}(\Phi) = H_{EB0}/\cos(\Phi - \Delta\Phi)$ with the field rotation angle Φ can be formulated to fit the angle-dependent H_{EB} (see detailed analysis in Note S4, Supporting Information), yielding a magnetization canting angle $\Delta\Phi$ of ≈ 10 degrees in CFGT (see also similar results from another device in Figure S4, Supporting Information). The canted magnetism is further confirmed by our DFT calculations and Monte Carlo simulations, which suggest that the intrinsic exchange bias and magnetocrystalline anisotropy energy of CFGT are the origin of canted magnetization (see detailed analysis in Note S5, Figures S5 and S6, Supporting Information).

2.2. Field-Free Spin-Orbit Torque Switching of CFGT/Pt Heterostructure Devices at Room Temperature

SOT phenomenon, which utilizes the spin-orbit interaction in materials and their hybrid structures with magnets, has emerged as an efficient method to control the magnetization in spintronic devices.^[3–5] For the success of SOT-driven magnetization dynamics,^[3–5] it is required to enhance the SOT efficiency, achieve magnetic field-free magnetization switching, and discover new materials and methods to control the device parameters^[2,6–16] (Figure 3a). To investigate the SOT-induced magnetization switching and dynamics in CFGT samples with intrinsic exchange bias and canted magnetization effects, CFGT/Pt heterostructure Hall bar devices were nanofabricated as shown in Figure 3b inset (see details in the Experimental section). For an effective SOT magnetization switching, it is essential to have a large charge-spin conversion efficiency in Pt

and high-quality CFGT/Pt interfaces for efficient transmission of spin current. In the SOT-induced magnetization switching experiment, a series of DC pulse currents I_p applied along the x-direction through the spin-orbit material (Pt), generates a spin current along the z-axis with spin polarization s_y along the y-axis due to the spin Hall effect. The resulting spin current exerts SOTs in CFGT (field-like τ_{FL} and damping-like τ_{DL} torques), enabling the switching of magnetization M direction. Specifically, the field-like torque $\tau_{FL} \approx M \times s_y$, precesses M about the exchange field created by spin polarization, while the damping-like torque $\tau_{DL} \approx M \times (M \times s_y)$ rotates the magnetization M toward the direction of spin polarization s_y . Typically, damping-like torque determines the switching of the magnetization.^[36]

The AHE signal of the CFGT/Pt Hall device shows an out-of-plane field magnetization and the difference of the switching field for both field sweep directions suggest a strong exchange bias ($H_{EB} = -35$ mT) in CFGT (Figure 3b). As shown in Figure 3c, we observed the SOT-induced magnetization switching using a pulsed write current I_p with pulse time 1 ms, followed by a small DC read current ($I_r \approx 50$ –500 μ A) to probe the magnetization state $R_{xy} = V_{xy}/I_r$. As the signal R_{xy} is proportional to the out-of-plane magnetization M_z ,^[41] the SOT R_{xy} signal shows current-induced magnetization change between $+M$ and $-M$. The magnitude change of R_{xy} in the SOT signal is almost the same as the AHE signal with field sweep, suggesting a full FM magnetization switch. Interestingly, we observe a deterministic SOT switching of CFGT at $H_x = 0$ T. This is in contrast to the conventional requirement of an in-plane magnetic field H_x to break the geometrical symmetry for a deterministic switching of the magnetization with a perpendicular magnetic anisotropy (PMA).^[37] To verify the origin, we performed SOT measurements with different in-plane magnetic fields H_x (Figure 3d). The H_x field does not affect the deterministic SOT switching, and the magnetization switching direction (chirality) remains the same in this field range of ± 500 mT, suggesting a robust deterministic switching against the external magnetic field due to the strong exchange bias effects and the canted magnetization of CFGT. The time-dependent switching experiments with different H_x were carried out (Figure 3e), further proving the reproducibility of the deterministic switching (also see reproducibility of SOT switching experiment Figures S7 and S8 (Supporting Information), discussion about the origin of the field-free SOT-induced magnetization switching in Note S6 (Supporting Information), and critical switching current density in Table S3, Supporting Information).

Conventionally, chirality is determined by the external field, which favors opposite switching directions for the positive and negative in-plane magnetic fields.^[37] If no external field is applied, the magnetization would be pulled to the in-plane orientation and broken into multiple domains, instead of the deterministic switching. However, in the canted magnetization scenario of the CFGT sample (Figure 3a, inset), the symmetry is broken as the easy axis of the magnetization M is canted at an angle $\Delta\Phi$ with respect to the normal direction. The damping-like torque τ_{DL} can rotate the M anticlockwise over the hard axis towards another easy axis, while the other rotation direction is not possible. This also explains the unchanged chirality of SOT switching with the external field direction, which is similar to that observed in other canted magnets.^[38] Thermal fluctuations induced by pulse current can randomize the magnetic domain

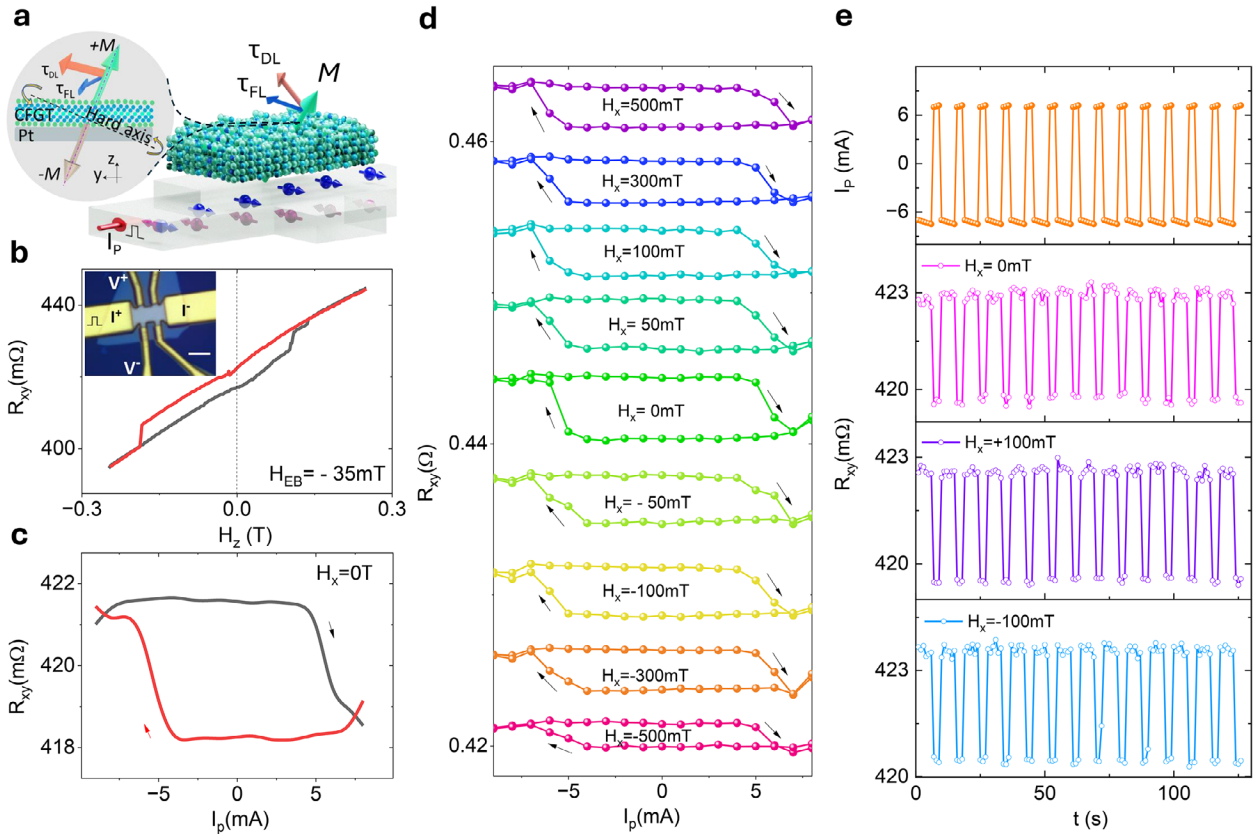


Figure 3. Field-free spin-orbit torque magnetization switching in CFGT/Pt heterostructure at room temperature. a) Schematics of CFGT/Pt van der Waals heterostructure used for pulsed current I_p -induced spin-orbit torque (SOT) experiments. Inset shows the mechanism of the field-free SOT switching of CFGT. b) AHE signals with an exchange field $H_{EB} = -35$ mT. The inset shows the optical microscope image of the CFGT/Pt heterostructure Hall-bar device. The scale bar is 2 μm . c, d) Pulsed write current I_p induced transverse Hall signal R_{xy} change due to SOT-induced magnetic switching without/with external in-plane magnetic field H_x . e) Time dependence of the pulse current I_p and the corresponding measured AHE signal R_{xy} with in-plane fields $H_x = 0$, and ± 100 mT. The pulse current dwell time is 1 ms and 3s waiting time before the reading process. All the measurements here were performed in Dev 1.

of CFGT and make switching behavior unstable.^[39] This is not the case in our CFGT/Pt SOT device, although the reduction of the SOT signal at a larger current due to thermal fluctuations cannot be ruled out.^[40] We can also rule out thermally assisted switching if the device reaches above T_c , as this can result in non-deterministic switching due to the formation of multiple domains.^[41,42] Therefore, the observed deterministic and field-free switching of CFGT can be attributed to the dominant SOT contribution and the canted magnetization of CFGT.

2.3. Estimation of Spin-Orbit Torque Magnetization Dynamics using 2nd Harmonic Hall Measurement in CFGT/Pt Heterostructure Devices

Harmonic Hall measurement is a powerful tool for studying different SOT contributions and effective spin-orbit fields in magnetic heterostructures.^[53] Application of an AC current $I_{ac} = I_0 \sin \omega t$ with frequency ω modulates the SOT amplitude and induces small oscillations of M about its equilibrium direction.^[44] Such oscillations generate a 2nd harmonic contribution to the Hall voltage^[54] ($V_{xy} \approx V_0 + V_{xy}^{1\omega} \sin \omega t + V_{xy}^{2\omega} \cos 2\omega t$), where V_{xy} de-

pends on M_z through the AHE and the product of $M_x \times M_y$ through the planar Hall effect (PHE). The 1st harmonic term $V_{xy}^{1\omega}$ relates to the equilibrium direction of the magnetization and is independent of the modulated SOT, which was measured as an in-phase ($\phi_{\text{lockin}} = 0^\circ$) signal. In the 1st harmonic Hall signals $V_{xy}^{1\omega}$ versus H_z field sweep (Figure 4a), we observed the expected AFM order transition and FM hysteresis in high and low field ranges, respectively, whereas the H_x field sweep measurement shows the FM magnetization component being pulled to the in-plane direction at around 2 T (i.e., magnetic anisotropy field, H_k), without any clear indication of the AFM transition up to 7 T.

The out-of-phase ($\phi_{\text{lockin}} = 90^\circ$) 2nd harmonic term $V_{xy}^{2\omega}$ measures the response of the magnetization to the current-induced spin-orbit fields. The current-induced effective field H_{eff} can be decomposed into two components: the field-like (H_{FL}) and damping-like (H_{DL}) spin-orbit fields, which can be extracted by the following equation,^[53]

$$V_{xy}^{2\omega} = - \left(V_{AHE} \frac{H_{DL}}{H - H_k} + V_{thermal} \right) \cos \varphi + 2V_{PHE} \frac{H_{FL} + H_{oe}}{H} (2\cos^3 \varphi - \cos \varphi) \quad (1)$$

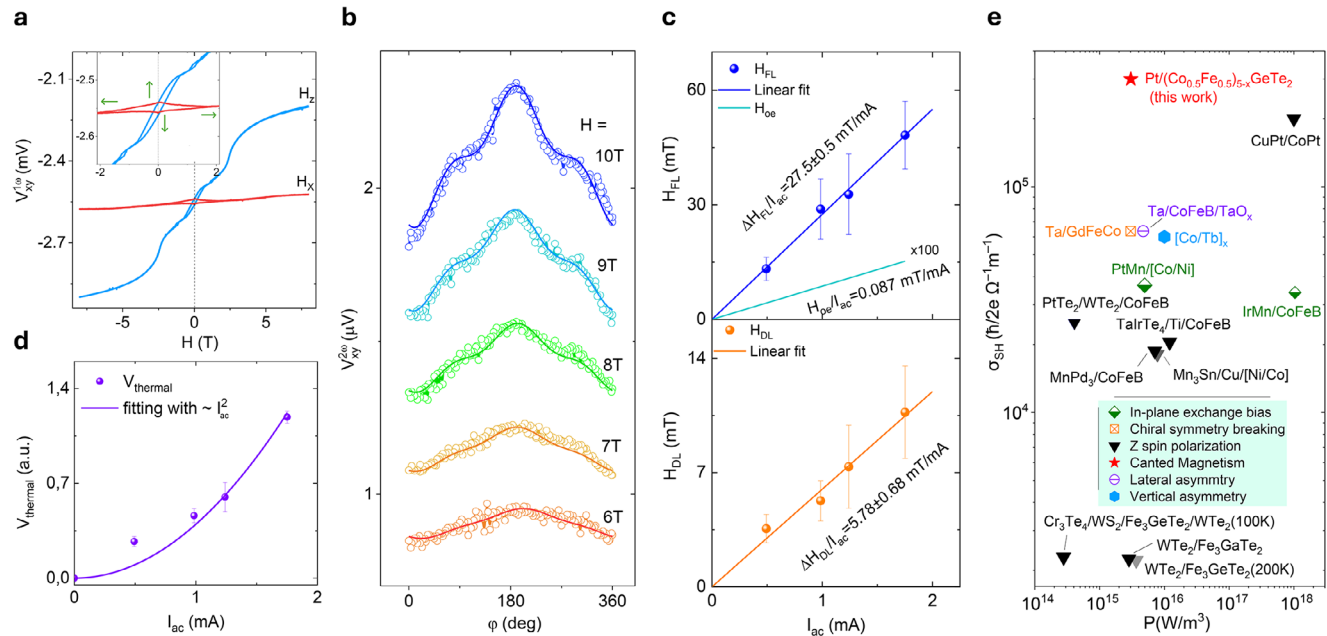


Figure 4. Harmonic Hall measurements of the CFGT/Pt Hall-bar device at room temperature. a) 1st harmonic $V_{xy}^{1\omega}$ signals as a function of the out-of-plane field H_z and in-plane field H_x sweeps. The inset is the zoom-in around 0 T. The green arrows show the FM components. b) In-plane angle φ dependence of the 2nd Harmonic signal $V_{xy}^{2\omega}$ at $I_{ac} = 1.75$ mA with in-plane field H . c, d) Extracted current dependence of the field-like effective field H_{FL} , Oersted field H_{Oe} , damping-like effective field H_{DL} , and thermal contribution. All the harmonic measurements were performed with $\omega = 213.14$ Hz at 300 K in Dev 2. e) Benchmarking our Pt-CFGT results with the state-of-the-art field-free magnetization switching devices reported in the literature such as PtMn/[Co/Ni],^[7] IrMn/CoFeB,^[8] Ta/GaFeCo,^[43] CuPt/CoPt,^[44] TaIrTe₄/Ti/CoFeB,^[16] PtTe₂/WTe₂/CoFeB,^[45] MnPd₃/CoFeB,^[46] Mn₃Sn/Cu/[Ni/Co],^[47] WTe₂/Fe₃GaTe₂,^[48] WTe₂/Fe₃GeTe₂,^[6] Cr₃Te₄/WS₂/Fe₃GeTe₂/WTe₂,^[49] Ta/CoFeB/TaOx,^[9] [Co/Tb]_x.^[50] Pt-based field assistant SOT devices: Pt/Fe₃GeTe₂,^[39,51] Pt/Fe₃GaTe₂.^[52] Spin Hall conductivity σ_{SH} as a function of the dissipation power density for magnetization switching $P = (J_{sw}^2/\sigma_c)$, where J_{sw} is the switching current density and σ_c is the conductance of the spin source material. Different field-free mechanisms are indicated with the symbols.

where H is the applied external field; φ is the angle between the applied current and the field. V_{AHE} and V_{PHE} are the AHE voltage and planar Hall (PHE) voltage, respectively. $V_{thermal}$ is the thermal-related contribution, like anomalous Nernst effect and spin Seebeck effect, etc. By adopting the simplified model,^[55] the current induced Oersted field $H_{Oe} = I_{Pt}/(2W)$ is also calculated, where W is the width of the Hall device. Therefore, the 2nd harmonic Hall voltage signal $V_{xy}^{2\omega}$ as a function of an in-plane rotation φ with fixed magnetic field H can be measured to extract the contributions from H_{DL} , H_{FL} , and the current-induced thermal effect (Figure 4b). Furthermore, the current dependence of the contributions from H_{DL} , H_{FL} , and the thermal effects are plotted in Figure 4c,d. We extracted $\Delta H_{DL}/J_{ac} = 4.2$ mT per MA/cm² with an effective saturation magnetization $\mu_0 M_s \approx 2.1$ emu cm⁻³ and $\Delta H_{FL}/J_{ac} = 19.7$ mT per MA cm⁻² (see more details on the harmonic Hall measurement methods in Note S7, Figures S10 and S11, Supporting Information, and the summary of the key SOT device parameters in Table S3, Supporting Information). The $\mu_0 M_s$ is smaller than the value of pure FM magnetic order with the AA' crystal structure.^[56] This suggests that the AFM order does not contribute much to the effective saturation magnetization even at large in-plane fields but coexists with the FM order, which agrees with the 1st harmonic result with H_x sweep.

The current-induced Oersted field is negligible and cannot be the origin of the field-free SOT-induced magnetization switch-

ing, while thermal contribution to the harmonic Hall voltage signal $V_{xy,thermal} \propto I^2$, increasing quadratically with the current, is proportional to M_x . Geometrically, $V_{xy,thermal} \approx M_x \times \nabla T_z$, where ∇T_z is due to the different thermal conductivity of CFGT, Pt, SiO₂/Si substrate, and air. Utilizing both SOT-induced magnetic switching and 2nd harmonic Hall measurements, we can conclude that the canted magnetization in CFGT can be efficiently controlled with a switching current density of $J_{sw} \approx 8 \times 10^6$ A cm⁻² at 300 K, which is lower than the reported values for vdW magnets.^[39,51,52] Moreover, as benchmarked against the state-of-the-art representative field-free SOT devices (Figure 4e), including devices with lateral asymmetry (mirror symmetry breaking), chiral symmetry breaking, in-plane exchange bias, vertical asymmetry, out-of-plane spin polarization S_z , Our Pt/CFGT devices show a very low operating power of $\approx 10^{15}$ W m⁻³ for the deterministic magnetization switching. Such highly efficient SOT-induced magnetization switching can be mainly due to the large spin Hall angle, high electrical conductance of Pt, and excellent spin transparency of the CFGT/Pt interface. Moreover, CFGT's lower conductivity compared to traditional 3D FMs such as Co and CoFeB enables a larger current to flow through the Pt, thereby enhancing energy efficiency. Noticeably, the $\sigma_{SH} (\approx 3 \times 10^5 \hbar/2e \Omega^{-1}m^{-1})$ of our device is comparable with other Pt-based field assistant SOT devices; however, it requires less power due to the small net magnetization $\mu_0 M_s$ of CFGT

(Figure 4e; also see state-of-the-art vdW magnet-based SOT devices in Note S8 and Figure S12a, Supporting Information). Alternatively, spin-orbit materials with lower crystal symmetry, such as WTe_2 and TaIrTe_4 , are used to deterministically switch the magnetization without an external field due to an out-of-plane SOT component.^[6,11,15,16,57] However, the unconventional SOT efficiency of WTe_2 and TaIrTe_4 from S_z spin component is still much smaller than that from S_y component of Pt.^[6,15,16,57] Therefore, the canted magnetism of CFGT enables a more energy-efficient and deterministic field-free SOT-induced magnetization switching in a heterostructure with Pt.

Importantly, for SOT memory devices, one of the traditional strategies is to utilize bilayers of FM/AFM thin films to achieve exchange bias and canted magnetism to realize field-free SOT magnetization switching, where AFM is just used as a pinned/exchange bias layer.^[7,8,19,58] However, our finding of the intrinsic coexistence of FM and AFM orders with exchange bias and canted magnetism in single magnetic materials CFGT enables us to demonstrate an energy-efficient and deterministic field-free SOT-induced magnetization switching of the vdW magnet CFGT. Furthermore, the low net magnetization of CFGT can also be useful for different device applications, for example, as shown for topological antiferromagnet Mn_3Sn ^[59] and compensated ferrimagnets (with almost zero magnetization) for ultrafast and energy-efficient switching.^[50,60–62]

3. Conclusion and Perspective

We observe the coexisting FM and AFM properties in vdW magnet CFGT much above room temperature, with intrinsic exchange bias and canted perpendicular ferromagnetism, which is not possible to attain in conventional systems. We understand the correlation between structural properties and coexisting magnetic orders using high-throughput DFT calculations utilizing data-driven analysis. It shows that such unique magnetic orders can be controlled by the positions of vacancies in the crystal and their symmetries, offering a new strategy for synthesizing novel vdW magnetic materials. Such intrinsic coexistence of non-trivial magnetic orders enables the demonstration of an energy-efficient, field-free, and deterministic switching of the vdW magnet CFGT in heterostructure with conventional material Pt with a large spin Hall conductivity. The detailed investigation of magnetic properties of CFGT and magnetization dynamics using SOT switching and 2nd harmonic Hall measurements of CFGT/Pt heterostructures show their relationship with the observed field-free SOT behavior. By demonstrating the feasibility of deterministic SOT-induced magnetization switching in a non-trivial vdW magnet at room temperature without the application of an external magnetic field, our work lays the foundation for the development of efficient spintronic devices based on vdW magnets. Moreover, intrinsically CFGT hosts both FM and AFM magnetic orders with a canted out-of-plane magnetism, offering the flexibility to combine other materials with even larger charge-spin conversion efficiency to enhance the device's performance.

4. Experimental Section

Device Fabrication: Single crystals of $(\text{Fe}_{0.5}\text{Co}_{0.5})_5\text{GeTe}_2$ (CFGT) were grown by chemical vapor transfer (CVT) method by HqGraphene. The AHE

measurements were measured in Hall-bar devices of CFGT (15–60 nm) on SiO_2/Si substrate. The CFGT crystal was exfoliated onto the SiO_2/Si wafer, followed by electron-beam lithography (EBL) and Ar plasma etching to pattern in a Hall-bar geometry, and the Au/Ti contacts were deposited 2nd EBL step and lift-off technique. The CFGT/Pt heterostructures were prepared by exfoliating thin CFGT crystals (15–60 nm) inside an N_2 glovebox onto pre-deposited Pt(10 nm)/Ti(2 nm) layers on a SiO_2/Si substrate. The Pt layer was prepared by electron-beam evaporation onto a Si/ SiO_2 substrate with a Ti seed layer. After exfoliation of CFGT, the samples were immediately transferred to an electron-beam evaporation system to deposit a 2 nm Al layer, forming an AlO_x capping layer. The Hall bar and contacts were patterned using EBL and Ar ion beam etching.

Electrical Measurements: Low temperature and high magnetic field measurements of CFGT Hall bar devices were performed in the Quantum Design cryogen-free PPMS DynaCool system with bias current in the range of 50–500 μA in the temperature range of 10–360 K and magnetic field up to 13 Tesla (T).

SOT Switching and Harmonic Measurements: SOT switching and Harmonic measurements in a low magnetic field range were carried out in a vacuum cryostat with a magnetic field up to 0.7 T for CFGT/Pt devices. The electronic measurements were performed using a Keithley 6221 current source, and a nanovoltmeter 2182A. To monitor the longitudinal and transverse Hall resistances, Keithley 2182A nanovoltmeters were utilized. For SOT-induced magnetization switching measurements, Keithley 2182A nanovoltmeters were used to monitor the response of the Hall resistances, while a Keithley 6221 AC source was utilized with a pulse current of 1 millisecond (ms) through the device, followed by a DC read current. The harmonic measurement was performed using Lockin SR830 to measure in-phase 1st and out-of-phase 2nd harmonic voltages, respectively. The 2nd harmonic measurements in the high magnetic field range were carried out in the Quantum Design cryogen-free PPMS DynaCool system with an external electronic connection to Lockin SR830 to measure the 1st and 2nd harmonic voltages.

SQUID Measurements: A Quantum Design superconducting quantum interference device (SQUID) was used to measure the static magnetic properties of bulk CFGT crystals. We measured the magnetization as a function of the out-of-plane ($H_{\parallel z}$) magnetic field. The bulk CFGT crystal was glued on a Si substrate to properly align the sample in the magnetic field during the measurements.

STEM Measurements: Scanning transmission electron microscopy (STEM) measurements were carried out using a JEOL monochromatic ARM200F transmission electron microscope (TEM), which is equipped with a Schottky field emission gun, a double-Wien monochromator, a probe Cs corrector and an image Cs corrector, as well as high angle annular dark field (HAADF) detectors for STEM imaging, a double silicon drift detector (SDD) for energy dispersive X-ray spectroscopy (EDXS), and a Gatan image filter (GIF) Continuum. The microscope was operated at 200 kV for HAADF STEM imaging. The beam convergence half-angle and inner collection half-angle for HAADF STEM are ≈ 27 mrad and ≈ 55 mrad, respectively. Specimens for STEM measurements were prepared by using a FEI Versa 3D focus ion beam–scanning electron microscope (FIB-SEM). After depositing a protection layer containing Pt and C using first the electron beam and then the Ga ion beam in the FIB-SEM, a lamella of the material was cut out using an ion beam at 30 kV and 1 nA. After transferring the lamella to a Cu TEM grid, the lamella was gradually thinned down by the ion beam. The thinning process was performed first at 30 kV and with a gradually decreasing beam current from 1 nA to 100 pA. Then, the gentle polishing of the specimen was carried out with an ion beam energy of 5 kV and 2 kV to minimize the ion beam effect.

Statistical Analysis: Statistical analysis was conducted using Python 3.12 with the libraries numpy, scipy.stats, and matplotlib. Outlier detection was performed using the interquartile range (IQR) method, and all data points—including identified outliers—were retained and visualized in the final boxplots to ensure full transparency. No transformation or normalization was applied. Data are presented using boxplots with overlaid individual data points. Each box displays the interquartile range (IQR; 25th to 75th percentile) with the median marked as a horizontal line. Whiskers extend to the most extreme values within $1.5 \times \text{IQR}$ from the lower and

upper quartiles. Points beyond the whiskers are plotted as outliers. Sample sizes were $n_1 = 100$ for Type I (AFM) and $n_2 = 100$ for Type II (FM). To assess the statistical significance in energy differences between the two compositions, the non-parametric Mann–Whitney U test was employed due to violations of normality. A statistically significant difference was found between the groups ($U = 8604.0$, $p = 1.31 \times 10^{-18}$), with the significance level set at $\alpha = 0.05$.

Supporting Information

Supporting Information is available from the Wiley Online Library or from the author.

Acknowledgements

Authors acknowledge funding from the European Innovation Council project 2DSPIN-TECH (No. 101135853), European Commission Graphene Flagship project, 2D TECH VINNOVA competence center (No. 2019-00068), Wallenberg Initiative Materials Science for Sustainability (WISE) funded by the Knut and Alice Wallenberg Foundation, EU Graphene Flagship (Core 3, No. 881603), Swedish Research Council (VR) grant (No. 2021–04821, No. 2018–07046), FLAG-ERA project 2DSOTECH (VR No. 2021–05925) and MagicTune, Graphene Center, Chalmers-Max IV collaboration grant, Areas of Advance (AoA) Nano, AoA Materials Science and AoA Energy programs at Chalmers University of Technology. The authors also acknowledge the help of staff at the Quantum Device Physics and Nanofabrication laboratory at Chalmers University of Technology. L.Z. and E.O. acknowledge the Swedish Research Council and Swedish Foundation for Strategic Research for access to ARTEMI, the Swedish National Infrastructure in Advanced Electron Microscopy (2021-00171 and RIF21-0026). This work was performed in part at the Chalmers Material Analysis Laboratory, CMAL. L.B. acknowledges the financial support from the Ministry of Electronics and Information Technology, India (No. 3149159). B.S. acknowledges financial support from the Swedish Research Council (grant no. 2022–04309 and grant No. 2018–07082). The computations were enabled by resources provided by the National Academic Infrastructure for Supercomputing in Sweden (NAISS) at UPPMAX (NAISS 2023/5-238) and at NSC and PDC (NAISS 2023/3-42), partially funded by the Swedish Research Council through grant agreement no. 2022–06725. B.S. also acknowledges the allocation of supercomputing hours in the EuroHPC Development Access Call (EHPC-DEV-2024D04-071) to EuroHPC resources in LUMI-C in Finland. [Correction added on July 29, 2025, after first online publication: Figure 1 has been updated.]

Conflict of Interest

The authors declare no conflict of interest.

Author Contributions

B.Z. and S.P.D. conceived the idea and designed the experiments. B.Z. fabricated and characterized the devices with some support from L.B. and R.N. S.E. and B.S. performed the theoretical calculations and data analysis. L.Z. and E.O. performed STEM characterization and data analysis. P.S. performed SQUID magnetization measurements and data analysis. B.Z., S.E., B.S. and S.P.D. analyzed and interpreted the data, compiled the figures, and wrote the manuscript with feedback from all co-authors. S.P.D. supervised and managed the research project.

Data Availability Statement

The data that support the findings of this study are available from the corresponding author upon reasonable request.

Keywords

($\text{Co}_{0.5}\text{Fe}_{0.5}$) $_{5-x}\text{GeTe}_2$, 2D magnets, anti-ferromagnet, exchange bias, ferromagnet, field-free magnetization switching, room temperature, spin-orbit torque

Received: February 11, 2025

Revised: June 14, 2025

Published online: July 1, 2025

- [1] X. Lin, W. Yang, K. L. Wang, W. Zhao, *Nat. Electron.* **2019**, *2*, 274.
- [2] H. Yang, S. O. Valenzuela, M. Chshiev, S. Couet, B. Dieny, B. Dlubak, A. Fert, K. Garello, M. Jamet, D.-E. Jeong, K. Lee, T. Lee, M.-B. Martin, G. S. Kar, P. S  n  r, H.-J. Shin, S. Roche, *Nature* **2022**, *606*, 663.
- [3] L. Liu, C.-F. Pai, Y. Li, H. W. Tseng, D. C. Ralph, R. A. Buhrman, *Science* **2012**, *336*, 555.
- [4] I. M. Miron, K. Garello, G. Gaudin, P.-J. Zermatten, M. V. Costache, S. Auffret, S. Bandiera, B. Rodmacq, A. Schuhl, P. Gambardella, *Nature* **2011**, *476*, 189.
- [5] A. Manchon, J. Zelezny, I. M. Miron, T. Jungwirth, J. Sinova, A. Thiaville, K. Garello, P. Gambardella, *Rev. Mod. Phys.* **2019**, *91*, 035004.
- [6] I.-H. Kao, R. Muzzio, H. Zhang, M. Zhu, J. Gobbo, S. Yuan, D. Weber, R. Rao, J. Li, J. H. Edgar, J. E. Goldberger, J. Yan, D. G. Mandrus, J. Hwang, R. Cheng, J. Katoch, S. Singh, *Nat. Mater.* **2022**, *21*, 1029.
- [7] S. Fukami, C. Zhang, S. DuttaGupta, A. Kurenkov, H. Ohno, *Nat. Mater.* **2016**, *15*, 535.
- [8] Y.-W. Oh, S.-H. Chris Baek, Y. M. Kim, H. Y. Lee, K.-D. Lee, C.-G. Yang, E.-S. Park, K.-S. Lee, K.-W. Kim, G. Go, J.-R. Jeong, B.-C. Min, H.-W. Lee, K.-J. Lee, B.-G. Park, *Nat. Nanotechnol.* **2016**, *11*, 878.
- [9] G. Yu, P. Upadhyaya, Y. Fan, J. G. Alzate, W. Jiang, K. L. Wong, S. Takei, S. A. Bender, L.-T. Chang, Y. Jiang, M. Lang, J. Tang, Y. Wang, Y. Tserkovnyak, P. K. Amiri, K. L. Wang, *Nat. Nanotechnol.* **2014**, *9*, 548.
- [10] B. Zhao, B. Karpiak, D. Khokhriakov, A. Johansson, A. Md. Hoque, X. Xu, Y. Jiang, I. Mertig, S. P. Dash, *Adv. Mater.* **2020**, *32*, 2000818.
- [11] L. Bainsla, B. Zhao, N. Behera, A. Md. Hoque, L. Sj  str  m, A. Martinelli, M. Abdel-Hafez, J.   kerman, S. P. Dash, *Nat. Commun.* **2024**, *15*, 4649.
- [12] T.-Y. Chen, H.-I. Chan, W.-B. Liao, C.-F. Pai, *Phys. Rev. Appl.* **2018**, *10*, 044038.
- [13] H.-J. Kim, K.-W. Moon, B. X. Tran, S. Yoon, C. Kim, S. Yang, J.-H. Ha, K. An, T.-S. Ju, J.-I. Hong, C. Hwang, *Adv. Funct. Mater.* **2022**, *32*, 2270153.
- [14] T. C. Chuang, C. F. Pai, S. Y. Huang, *Phys. Rev. Appl.* **2019**, *11*, 61005.
- [15] Y. Zhang, H. Xu, K. Jia, G. Lan, Z. Huang, B. He, C. He, Q. Shao, Y. Wang, M. Zhao, T. Ma, J. Dong, C. Guo, C. Cheng, J. Feng, C. Wan, H. Wei, Y. Shi, G. Zhang, X. Han, G. Yu, *Sci. Adv.* **2023**, *9*, adg981.
- [16] Y. Liu, G. Shi, D. Kumar, T. Kim, S. Shi, D. Yang, J. Zhang, C. Zhang, F. Wang, S. Yang, Y. Pu, P. Yu, K. Cai, H. Yang, *Nat. Electron* **2023**, *6*, 732.
- [17] B. Zhao, L. Pandey, K. Ali, E. Wang, C. M. Polley, B. Thiagarajan, P. Makk, M. H. D. Guimar  es, S. P. Dash, *ACS Nano* **2025**, *19*, 13817.
- [18] S. Peng, D. Zhu, W. Li, H. Wu, A. J. Grutter, D. A. Gilbert, J. Lu, D. Xiong, W. Cai, P. Shafer, K. L. Wang, W. Zhao, *Nat. Electron.* **2020**, *3*, 757.
- [19] T. M. J. Cham, R. J. Dorrian, X. S. Zhang, A. H. Dismukes, D. G. Chica, A. F. May, X. Roy, D. A. Muller, D. C. Ralph, Y. K. Luo, *Adv. Mater.* **2023**, *36*, 2305739.
- [20] H. Kurebayashi, J. H. Garcia, S. Khan, J. Sinova, S. Roche, *Nat. Rev. Phys.* **2022**, *4*, 150.
- [21] B. Huang, M. A. McGuire, A. F. May, D. Xiao, P. Jarillo-Herrero, X. Xu, *Nat. Mater.* **2020**, *19*, 1276.

- [22] B. Zhao, R. Ngalyo, S. Ghosh, S. Ershadrad, R. Gupta, K. Ali, A. Md. Hoque, B. Karpiak, D. Khokhriakov, C. Polley, B. Thiagarajan, A. Kalaboukhov, P. Svedlindh, B. Sanyal, S. P. Dash, *Adv. Mater.* **2023**, 35, 2209113.
- [23] K. F. Mak, J. Shan, D. C. Ralph, *Nat. Rev. Phys.* **2019**, 1, 646.
- [24] K. S. Burch, D. Mandrus, J.-G. Park, *Nature* **2018**, 563, 47.
- [25] R. Ngalyo, B. Zhao, S. Ershadrad, R. Gupta, M. Davoudiniya, L. Bainsla, L. Sjöström, Md. A. Hoque, A. Kalaboukhov, P. Svedlindh, B. Sanyal, S. P. Dash, *ACS Nano* **2024**, 18, 5248.
- [26] C. Tian, F. Pan, S. Xu, K. Ai, T. Xia, P. Cheng, *Appl. Phys. Lett.* **2020**, 116, 202402.
- [27] A. F. May, M.-H. Du, V. R. Cooper, M. A. McGuire, *Phys. Rev. Mater.* **2020**, 4, 074008.
- [28] Y. Liu, V. N. Ivanovski, C. Petrovic, *Phys. Rev. B* **2017**, 96, 144429.
- [29] Z. Li, W. Xia, H. Su, Z. Yu, Y. Fu, L. Chen, X. Wang, N. Yu, Z. Zou, Y. Guo, *Sci. Rep.* **2020**, 10, 15345.
- [30] H. Zhang, Y.-T. Shao, R. Chen, X. Chen, S. Susarla, D. Raftrey, J. T. Reichanadter, L. Caretta, X. Huang, N. S. Settineri, Z. Chen, J. Zhou, E. Bourret-Courchesne, P. Ercius, J. Yao, P. Fischer, J. B. Neaton, D. A. Muller, R. J. Birgeneau, R. Ramesh, *Phys. Rev. Mater.* **2022**, 6, 044403.
- [31] G. Zhang, F. Guo, H. Wu, X. Wen, L. Yang, W. Jin, W. Zhang, H. Chang, *Nat. Commun.* **2022**, 13, 5067.
- [32] A. F. May, D. Ovchinnikov, Q. Zheng, R. Hermann, S. Calder, B. Huang, Z. Fei, Y. Liu, X. Xu, M. A. McGuire, *ACS Nano* **2019**, 13, 4436.
- [33] Y. Deng, Y. Yu, Y. Song, J. Zhang, N. Z. Wang, Z. Sun, Y. Yi, Y. Z. Wu, S. Wu, J. Zhu, J. Wang, X. H. Chen, Y. Zhang, *Nature* **2018**, 563, 94.
- [34] M. Huang, Z. Ma, S. Wang, S. Li, M. Li, J. Xiang, P. Liu, G. Hu, Z. Zhang, Z. Sun, Y. Lu, Z. Sheng, G. Chen, Y. Chueh, S. A Yang, B. Xiang, *2D Mater.* **2021**, 8, 031003.
- [35] D. R. Klein, D. MacNeill, J. L. Lado, D. Soriano, E. Navarro-Moratalla, K. Watanabe, T. Taniguchi, S. Manni, P. Canfield, J. Fernández-Rossier, P. Jarillo-Herrero, *Science* **2018**, 360, 1218.
- [36] S. Zhang, P. M. Levy, A. Fert, *Phys. Rev. Lett.* **2002**, 88, 236601.
- [37] L. Liu, O. J. Lee, T. J. Gudmundsen, D. C. Ralph, R. A. Buhrman, *Phys. Rev. Lett.* **2012**, 109, 096602.
- [38] L. Liu, Q. Qin, W. Lin, C. Li, Q. Xie, S. He, X. Shu, C. Zhou, Z. Lim, J. Yu, W. Lu, M. Li, X. Yan, S. J. Pennycook, J. Chen, *Nat. Nanotechnol.* **2019**, 14, 939.
- [39] X. Wang, J. Tang, X. Xia, C. He, J. Zhang, Y. Liu, C. Wan, C. Fang, C. Guo, W. Yang, Y. Guang, X. Zhang, H. Xu, J. Wei, M. Liao, X. Lu, J. Feng, X. Li, Y. Peng, H. Wei, R. Yang, D. Shi, X. Zhang, Z. Han, Z. Zhang, G. Zhang, G. Yu, X. Han, *Sci. Adv.* **2019**, 5, aaw8904.
- [40] I. Shin, W. J. Cho, E.-S. An, S. Park, H.-W. Jeong, S. Jang, W. J. Baek, S. Y. Park, D.-H. Yang, J. H. Seo, G.-Y. Kim, M. N. Ali, S.-Y. Choi, H.-W. Lee, J. S. Kim, S. D. Kim, G.-H. Lee, *Adv. Mater.* **2022**, 34, 2101730.
- [41] G. K. Krishnaswamy, G. Sala, B. Jacot, C.-H. Lambert, R. Schlitz, M. D. Rossell, P. Noël, P. Gambardella, *Phys. Rev. Appl.* **2022**, 18, 024064.
- [42] B. Pal, B. K. Hazra, B. Göbel, J.-C. Jeon, A. K. Pandeya, A. Chakraborty, O. Busch, A. K. Srivastava, H. Deniz, J. M. Taylor, H. Meyerheim, I. Mertig, S.-H. Yang, S. S. P. Parkin, *Sci. Adv.* **2022**, 8, abo5930.
- [43] H. Wu, J. Nance, S. A. Razavi, D. Lujan, B. Dai, Y. Liu, H. He, B. Cui, D. Wu, K. Wong, K. Sobotkiewich, X. Li, G. P. Carman, K. L. Wang, *Nano Lett.* **2021**, 21, 515.
- [44] L. Liu, C. Zhou, X. Shu, C. Li, T. Zhao, W. Lin, J. Deng, Q. Xie, S. Chen, J. Zhou, R. Guo, H. Wang, J. Yu, S. Shi, P. Yang, S. Pennycook, A. Manchon, J. Chen, *Nat. Nanotechnol.* **2021**, 16, 277.
- [45] F. Wang, G. Shi, K.-W. Kim, H.-J. Park, J. G. Jang, H. R. Tan, M. Lin, Y. Liu, T. Kim, D. Yang, S. Zhao, K. Lee, S. Yang, A. Soumyanarayanan, K.-J. Lee, H. Yang, *Nat. Mater.* **2024**, 23, 768.
- [46] M. DC, D.-F. Shao, V. D.-H. Hou, A. Vailionis, P. Quarterman, A. Habiboglu, M. B. Venuti, F. Xue, Y.-L. Huang, C.-M. Lee, M. Miura, B. Kirby, C. Bi, X. Li, Y. Deng, S.-J. Lin, W. Tsai, S. Eley, W.-G. Wang, J. A. Borchers, E. Y. Tsymbal, S. X. Wang, *Nat. Mater.* **2023**, 22, 591.
- [47] S. Hu, D.-F. Shao, H. Yang, C. Pan, Z. Fu, M. Tang, Y. Yang, W. Fan, S. Zhou, E. Y. Tsymbal, X. Qiu, *Nat. Commun.* **2022**, 13, 4447.
- [48] S. N. Kajale, T. Nguyen, N. T. Hung, M. Li, D. Sarkar, *Sci. Adv.* **2024**, 10, adk8669.
- [49] K. He, B. Li, J. Nie, Y. Hou, C. Huan, M. Hong, J. Du, Y. Chen, J. Tang, C. Yi, Y. Feng, S. Liu, S. Wu, M. Liu, H. Zhang, Y. Guo, R. Wu, J. Li, X. Liu, Y. Liu, Z. Wei, L. Liao, B. Li, X. Duan, *Adv. Mater.* **2025**, 37, 2419939.
- [50] Z. Zhang, Y. Zhang, V. Lopez-Dominguez, L. Sánchez-Tejerina, J. Shi, X. Feng, L. Chen, Z. Wang, Z. Zhang, K. Zhang, B. Hong, Y. Xu, Y. Zhang, M. Carpentieri, A. Fert, G. Finocchio, W. Zhao, P. Khalili Amiri, *Nat. Commun.* **2021**, 12, 4555.
- [51] M. Alghamdi, M. Lohmann, J. Li, P. R. Jothi, Q. Shao, M. Aldosary, T. Su, B. P. T. Fokwa, J. Shi, *Nano Lett.* **2019**, 19, 4400.
- [52] W. Li, W. Zhu, G. Zhang, H. Wu, S. Zhu, R. Li, E. Zhang, X. Zhang, Y. Deng, J. Zhang, L. Zhao, H. Chang, K. Wang, *Adv. Mater.* **2023**, 35, 2303688.
- [53] M. Hayashi, J. Kim, M. Yamanouchi, H. Ohno, *Phys. Rev. B* **2014**, 89, 144425.
- [54] C. O. Avci, K. Garello, M. Gabureac, A. Ghosh, A. Fuhrer, S. F. Alvarado, P. Gambardella, *Phys. Rev. B* **2014**, 90, 224427.
- [55] M. DC, R. Grassi, J.-Y. Chen, M. Jamali, D. Reifsnnyder Hickey, D. Zhang, Z. Zhao, H. Li, P. Quarterman, Y. Lv, M. Li, A. Manchon, K. A. Mkhoyan, T. Low, J.-P. Wang, *Nat. Mater.* **2018**, 17, 800.
- [56] H. Zhang, D. Raftrey, Y.-T. Chan, Y.-T. Shao, R. Chen, X. Chen, X. Huang, J. T. Reichanadter, K. Dong, S. Susarla, L. Caretta, Z. Chen, J. Yao, P. Fischer, J. B. Neaton, W. Wu, D. A. Muller, R. J. Birgeneau, R. Ramesh, *Sci. Adv.* **2022**, 8, abm7103.
- [57] D. MacNeill, G. M. Stiehl, M. H. D. Guimaraes, R. A. Buhrman, J. Park, D. C. Ralph, *Nat. Phys.* **2017**, 13, 300.
- [58] S.-H. C. Baek, V. P. Amin, Y.-W. Oh, G. Go, S.-J. Lee, G.-H. Lee, K.-J. Kim, M. D. Stiles, B.-G. Park, K.-J. Lee, *Nat. Mater.* **2018**, 17, 509.
- [59] H. Tsai, T. Higo, K. Kondou, T. Nomoto, A. Sakai, A. Kobayashi, T. Nakano, K. Yakushiji, R. Arita, S. Miwa, Y. Otani, S. Nakatsuji, *Nat.* **2020**, 580, 608.
- [60] K. Cai, Z. Zhu, J. M. Lee, R. Mishra, L. Ren, S. D. Pollard, P. He, G. Liang, K. L. Teo, H. Yang, *Nat. Electron.* **2020**, 3, 37.
- [61] H. Wu, Y. Xu, P. Deng, Q. Pan, S. A. Razavi, K. Wong, L. Huang, B. Dai, Q. Shao, G. Yu, X. Han, J.-C. Rojas-Sánchez, S. Mangin, K. L. Wang, *Adv. Mater.* **2019**, 31, 1901681.
- [62] J. Yu, D. Bang, R. Mishra, R. Ramaswamy, J. H. Oh, H.-J. Park, Y. Jeong, P. Van Thach, D.-K. Lee, G. Go, S.-W. Lee, Y. Wang, S. Shi, X. Qiu, H. Awano, K.-J. Lee, H. Yang, *Nat. Mater.* **2019**, 18, 29.